Available online at www.sciencedirect.com

SCIENCE DIRECT®

Developmental Biology 271 (2004) 210–222

DEVELOPMENTAL BIOLOGY

www.elsevier.com/locate/ydbio

Multicellular computer simulation of morphogenesis: blastocoel roof thinning and matrix assembly in *Xenopus laevis*

Diane Longo,[a,1] Shayn M. Peirce,[a,*,1] Thomas C. Skalak,[a] Lance Davidson,[b,c] Mungo Marsden,[c] Bette Dzamba,[c] and Douglas W. DeSimone[c,d]

[a] *Department of Biomedical Engineering, University of Virginia, Charlottesville, VA 22908, USA*
[b] *Department of Biology, University of Virginia, Charlottesville, VA 22908, USA*
[c] *Department of Cell Biology, University of Virginia Health System, School of Medicine, Charlottesville, VA 22908, USA*
[d] *Morphogenesis and Regenerative Medicine Institute, University of Virginia Health System, School of Medicine, Charlottesville, VA 22908, USA*

Received for publication 14 September 2003, revised 18 February 2004, accepted 9 March 2004

Available online 7 May 2004

Abstract

In the blastocoel roof (BCR) of the *Xenopus laevis* embryo, epibolic movements are driven by the radial intercalation of deep cell layers and the coordinate spreading of the overlying superficial cell layer. Thinning of the lateral margins of the BCR by radial intercalation requires fibronectin (FN), which is produced and assembled into fibrils by the inner deep cell layer of the BCR. A cellular automata (CA) computer model was developed to analyze the spatial and temporal movements of BCR cells during epiboly. Simulation parameters were defined based on published data and independent results detailing initial tissue geometry, cell numbers, cell intercalation rates, and migration rates. Hypotheses regarding differential cell adhesion and FN assembly were also considered in setting system parameters. A 2-dimensional model simulation was developed that predicts BCR thinning time of 4.8 h, which closely approximates the time required for the completion of gastrulation in vivo. Additionally, the model predicts a temporal increase in FN matrix assembly that parallels fibrillogenesis in the embryo. The model is capable of independent predictions of cell rearrangements during epiboly, and here was used to predict successfully the lateral dispersion of a patch of cells implanted in the BCR, and increased assembly of FN matrix following inhibition of radial intercalation by N-cadherin over-expression.

Keywords: Blastocoel roof; Fibronectin; Cellular automata; Epiboly; Computational model; Morphogenesis

Introduction

The establishment and maintenance of epithelial cell sheets are critical for embryonic development, organogenesis, and wound healing (Jacinto et al., 2001; Martin and Wood, 2002; Simske and Hardin, 2001). The thinning of multilayered epithelia is a dramatic but poorly understood form of epithelial sheet morphogenesis. One of the best characterized examples of epithelial thinning occurs during the process of epiboly in *Xenopus laevis* embryos. Before the onset of gastrulation movements (late stage 8; Nieuwkoop and Faber, 1967), the *Xenopus* blastocoel roof (BCR) is three to four cell layers thick in the animal pole of the embryo (and five to six layers thick in the lateral margins of the BCR). The outermost superficial layer of cells is a true epithelium while the inner "deep" cell layers are free to intercalate (Chalmers et al., 2003). As development of the embryo progresses, the three to six deep cell layers rearrange into two layers by radial intercalation, which involves the interdigitation of cells along the radius of the embryo (Fig. 1). During this process, fibronectin (FN) is deposited and assembled into fibrils (fibrillogenesis) at the interface of the inner layer of cells and the blastocoel (Winklbauer and Stoltz, 1995). The FN matrix is thought to play an instructive role in the lateral BCR thinning process, possibly by affecting the polarity of cells undergoing these behaviors (Marsden and DeSimone, 2001).

Although the movements of individual cells in the BCR have been described (Keller, 1978, 1980), the cellular mechanisms underlying these behaviors have not been

* Corresponding author. Department of Biomedical Engineering, University of Virginia, Box 800759, Health System, Charlottesville, VA 22908. Fax: +1-434-982-3870.
E-mail address: smp6p@virginia.edu (S.M. Peirce).
[1] These authors contributed equally to this work.

0012-1606/$ - see front matter © 2004 Elsevier Inc. All rights reserved.
doi:10.1016/j.ydbio.2004.03.021

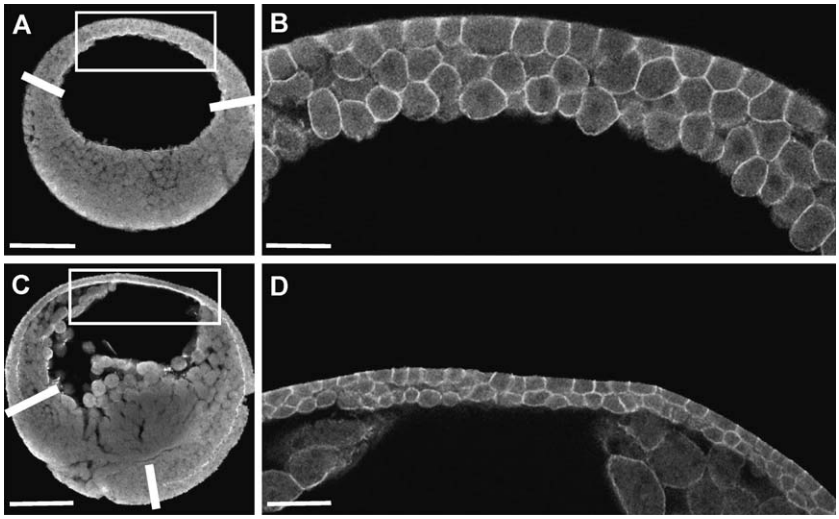

Fig. 1. The BCR thins during gastrulation. Confocal micrographs of bisected early (Stage 9, A and B) and late (Stage 11.5, C and D) *Xenopus laevis* gastrula stage embryos. At the beginning of gastrulation (A and B), the roof consists of an outer layer of epithelial cells and 2–3 layers of deep cells. Near the end of gastrulation (C and D), the deep layers have radially intercalated so that the roof is composed of only two layers of cells: the superficial epithelial cells and one layer of deep cells. During gastrulation, FN is assembled under the BCR cells. Boxes indicate the center of the BCR. Underlying mesoderm has migrated along the inner surface of the roof in C and D but is easily distinguished by the line of FN staining that separates the BCR from the mesoderm (C). (B and D) Higher magnification images of similar regions of the BCR to those boxed in A and C, cell outlines visualized using antisera to C-cadherin (scale bars = 300 μm in A and C; scale bars = 75 μm in B and D). The area between the white bars in A and C represents the area modeled in the CA simulation. The area outlined by the box is shown at higher magnification in B and D, and represents the center portion (which is 3-cell layers thick) of what was actually modeled.

revealed. One way to acquire a greater comprehension of the cellular mechanisms responsible for BCR thinning is to utilize an integrated systems approach. Conventional molecular-genetic strategies target the functions of a particular molecule or pathway and anticipate observable changes in the functionality or architecture of an organism, tissue, or cell. However, because cell–cell interactions typically involve multiple signals acting at specific tissue locations and at specific times, the ability to sort out possible functional effects of multiple single gene perturbations is easily overwhelmed. A new scientific approach, variously termed "integrative biology", "computational biology", or "in silico biology"—refers to a range of strategies in which genomic and proteomic information is integrated via computational analysis to gain insight into complex system behaviors and to help in the design of experiments for the independent verification of new concepts (Peirce et al., 2004; von Dassow et al., 2000).

Advances in molecular biology and genetics make it tempting to speculate that collective knowledge of the spatial and temporal expression patterns and functions of individual genes will enable a complete understanding of morphogenetic processes (Metzger and Krasnow, 1999). Computational models have the power to integrate spatial and temporal features of gene and protein expression patterns, cell–cell and cell–matrix signaling processes, and cellular movements to generate useful functional knowledge not otherwise attainable through experimental studies alone. Previous computational models that have been developed to study morphogenetic phenomena have used a variety of techniques including geometrical analysis (Honda, 1983), finite element analysis (Brodland and Chen, 2000; Brodland and Clausi, 1994), finite difference analysis (Weliky and Oster, 1990; Weliky et al., 1991), and continuum theory (Meinhardt and Gierer, 1980; Murray and Oster, 1984; Ngwa and Maini, 1995). von Dassow et al. (2000) recently demonstrated the usefulness of the computational approach by exploring the set of solutions for a system of molecular interactions in which all parameters are not independently known. The result was a new insight into a signaling loop operating between two types of cells in the *Drosophila* embryo that is required to achieve the appropriate final arrangement of cells. More recently, a cell-based simulation was developed by Zajac et al. (2003) to study convergent extension in *Xenopus laevis* development. Simulations were based on differential adhesion of cells and small energy changes, which caused cells with probabilistic displacements of their boundaries to undergo realistic assembly (Zajac et al., 2003).

The main objective of the current study was to develop a 2-dimensional cellular automata (CA) simulation of embryonic tissue morphogenesis. In contrast to previous computational models, however, this CA model integrates defined variables and rules obtained from published and independent experimental data and allows for the autonomous movements and interactions of hundreds of cells in response to changes in tissue environment. The CA model of BCR thinning produced realistic emergent morphogenetic cell motions and FN deposition and assembly, thus recapitulating two aspects of in vivo BCR thinning. We find, therefore, that application of a cell-based computational technique to the process of BCR thinning may help reveal information

that cannot be obtained solely through experimental observation and/or manipulation of the *X. laevis* embryo.

Materials and methods

Embryo culture and microsurgery

Embryos were obtained by standard methods (Kay and Peng, 1991) and staged according to Nieuwkoop and Faber (1967). Albino embryos were cultured in 0.33× modified Barth's solution (MBS). To enhance contrast of implanted deep cells, 2.0 nl of a 25 mg/ml stock of a fluorescent lineage tracer was injected (Alexa fluorescein 488 dextran amine; Molecular Probes, Eugene) at the one cell stage. Vitelline membranes were removed with forceps and microsurgery was carried out using hair-loops and eyebrow hair-knives in Danilchik's For Amy (DFA; 53 mM NaCl, 5 mM Na2CO3, 4.5 mM K Gluconate, 32 mM Na Gluconate, 1 mM CaCl2, 1 mM MgSO4, 0.1% bovine serum albumen (BSA)), buffered to pH 8.3 with Bicine (Sater et al., 1993). Antibiotic/antimycotic (Sigma; 0.1 U penicillin, 0.1 mg streptomycin, and 0.25 μg amphotericin B per ml) was added to DFA. Microsurgery and subsequent culture of host embryos were carried out in clay-lined Petri dishes. To graft fluorescently labeled cells from a labeled donor into a host embryo an uninjected host and a labeled embryo were selected at stage 8. A "flap" was cut through the single-cell layer of the epithelium and peeled back on both the host and donor embryos. A small patch of 5 to 10 cells was cut from the labeled donor and placed under the flap of the unlabeled host and the flap was held in place with a small coverslip fragment. After 30 min, DFA was replaced by 0.33× MBS supplemented with antibiotic/antimycotic and BSA and the coverslip fragment was removed.

Histology

Embryos in Fig. 1 were fixed in 2% trichloroacetic acid in 1× MBS and bisected with a scalpel. Bisected embryos were stained with an antiserum to FN or to C-cadherin (a gift from Barry Gumbiner), followed by an Alexafluor 488 conjugated anti-rabbit IgG secondary antibody. Stained embryos were cleared and mounted in Murray's clear and photographed using a Nikon C1 confocal microscope. To resolve details of the distribution of implanted cells host embryos were fixed overnight at 4°C in MEMFA (0.1 M MOPS pH 7.4, 2 mM EGTA, 1 mM MgSO4, and 3.7% Formaldehyde). The animal cap was excised from fixed embryos with a scalpel and mounted in Murray's Clear (Sive et al., 2000).

Microscopy and imaging

Live images of fluorescently labeled cell implants were collected with a digital CCD camera (Hamamatsu Corp.) mounted on a fluorescence-equipped stereoscope (Olympus). Confocal z-sections of fixed samples were collected with a laser-scanning confocal microscope (PCM2000; Nikon) mounted on an inverted compound microscope (Nikon) using a 20× oil objective. Confocal z-series were processed into single projected images using image analysis software (ImageJ; Wayne Rasband, Research Services Branch, National Institute of Mental Health, Bethesda, MD, USA; available for download at http://www.rsb.info.nih.gov/ij/). Subsequent manipulations of images were carried out with image manipulation software (Adobe Photoshop).

Measurements and observations from X. laevis embryos

The initial description of the morphogenetic movements that occur during *X. laevis* development was obtained from previously published work: the BCR thinning event in the *X. laevis* is caused by the radial intercalation of deep layer cells (Keller, 1980). Radial intercalation continues until the BCR consists of two cell layers: one layer of superficial cells and one layer of deep or inner cells. The BCR thins to two layers between stages 8 and 12, a time span of approximately 4 h (Keller, 1980). A matrix of FN fibrils forms on the inner layer of BCR cells during the thinning event (Winklbauer and Stoltz, 1995). Without the presence of a FN matrix, the cellular rearrangements that occur during thinning are not maintained (Marsden and DeSimone, 2001).

Measuring FN content at stages 9, 10, 11, and 12

To observe FN on the BCR, embryos were fixed in 2% trichloroacetic acid, and then bisected with a scalpel. Bisected embryos were stained with an antiserum to FN (PcAb 32), followed by an Alexafluor 488 conjugated anti-rabbit IgG secondary antibody. Stained embryos were photographed using a Nikon C1 confocal microscope. Scan times were held constant for all stages. The FN intensity at stages 9, 10, 11, and 12 was quantified by using Scion Image software to analyze four sets of images from each stage. FN content was determined by measuring the absolute integrated density per cell and calculating the mean for each stage.

Cadherin expression studies

Transcripts encoding full-length *Xenopus* N-Cadherin were synthesized in vitro from the N-cadherin PCS2 + MT cDNA plasmid (gift from Dr. Chris Kintner) using standard methods (Sive et al., 2000). Transcripts (250 pg/embryo) were injected into the animal pole of 1 blastomere at the 2-cell stage. Embryos were processed for immunolocalization and confocal microscopy as described above. FN matrix accumulation was detected using PcAb 32 and cells expressing the myc-tagged N-cadherin were detected using mAb 9E10 (Evan et al., 1985). Additional details are reported in Dzamba and DeSimone (in preparation).

Measuring the dilution of the bottom cell layer

An embryo explant seeded on an FN substrate containing labeled bottom deep cells and unlabeled intercalating cells was monitored over time (Marsden and DeSimone, 2001). The number of cells that intercalated into the bottom deep layer in the first hour of intercalation was counted, and this number was converted to a dilution rate based on the total number of cells in the bottom deep layer.

Running the simulation and collecting data

The simulation was run in the NetLogo environment (Wilensky, U. (1999). NetLogo. http://www.ccl.northwestern.edu/netlogo. Center for Connected Learning and Computer-Based Modeling. Northwestern University, Evanston, IL). Simple algorithms were generated to collect data such as total thinning time, temporal FN values, and cell locations. The data were exported to Microsoft Excel for analysis.

Statistical analysis

Differences in mean data between samples were compared using Student's *t* tests, and differences were considered significant at $P < 0.05$.

Results

To build the CA simulation, we defined the cells, cell layers, and tissue organization in the simulation and incorporated rules for cell behaviors based on independent experimental work published in the literature and our own unpublished experimental observations. To test the predictive capability of the CA model, we compared the spatial patterns of cellular rearrangement and tissue layer morphology, as well as the temporal dynamics of BCR thinning predicted by the model to those measured in independent experimental studies. To further assess the predictive value of the CA model and establish the robustness of the computational approach, we simulated implantations of labeled donor cells into recipient BCRs and tracked the lateral dispersions of these cells throughout the virtual BCR. We compared the predicted results to those generated by performing the same experimental manipulation in vivo. Finally, we used the CA simulation to test the hypothesis that FN deposition and fibrillogenesis at BCR cell surfaces are influenced by differential cell adhesion and cell residency times in the BCR.

Building the simulation

The NetLogo modeling tool was used to develop the computer simulation of the BCR thinning process. Net-

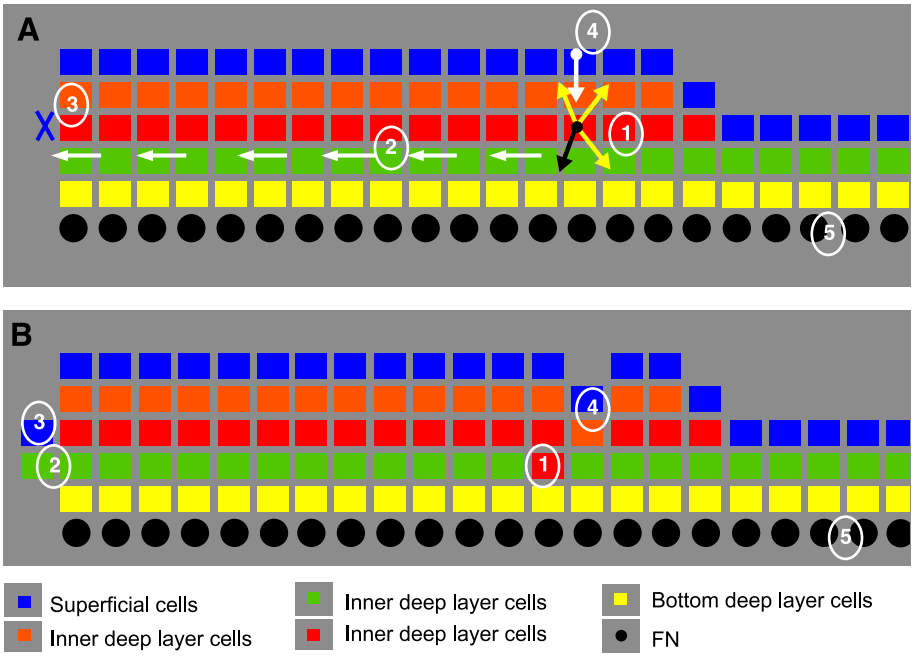

Fig. 2. Cellular behavior is governed by the set of rules incorporated in the simulation. (A) This diagram represents a sequence of cell movements and actions that are possible given the defined set of rules: (1) an inner deep layer cell is selected at random to move. The black arrow and the three yellow arrows emanating from the selected cell represent the possible directions the cell can move in. The black arrow represents the randomly selected direction. The red cell intercalates between the two green cells on either side of the black arrow, (2) all of the green cells to the left of the intercalated red cell are displaced one cell diameter to the left, (3) the superficial cell layer extends (spreads) to cover the protruding green cell layer, (4) an orange deep cell drops down to fill the gap created by the intercalated red cell. The superficial cell layer conforms to fill the gap created by the orange cell, (5) the FN intensity associated with each bottom (yellow) deep layer cell is incremented if the residency time and cell-to-cell contact criteria are met. (B) The tissue geometry after the events described in (A) have occurred.

Logo is a programmable modeling package that was developed for the purpose of simulating complex, multi-component systems. In the CA simulation of BCR thinning, hundreds of individual cells in the BCR interact and the emergent behavior is the thinning of the BCR into two cell layers. The computer model simulates a network of approximately 300 cells in the region bounded by the white bars in Fig. 1A, including the area within the box. The edges of the initial region of interest within the BCR are five cell layers thick, and the middle is three cell layers thick. The length of the modeled region is approximately 2100 μm (84 cells long, 25 μm/cell). The model contains two main cell types: superficial or epithelial cells and deep cells. Deep cells in the bottom cell layer are capable of depositing FN at the cell surface and assembling a matrix of FN fibrils (Fig. 2). The model contains an FN layer that is a gray-scaled representation of FN intensity, and in Fig. 2, this layer is represented by black circles.

There are multiple rules that govern the behavior of individual cells (Table 1), each derived from independent experiments. For example, individual cell movements are dictated by a distinct set of rules (Fig. 2). At each time step, an inner deep cell is selected at random to move. The inner deep layer cells can intercalate into an upper or lower layer of deep cells. If an inner deep cell intercalates into the bottom deep cell layer, the cell is "captured" by the bottom cell layer. Cells in the bottom deep cell layer are confined to this layer and cannot intercalate into another cell layer (Marsden and DeSimone, 2001). However, cells in the bottom layer are displaced to the left and to the right as cells from upper layers intercalate into the bottom cell layer. As cells intercalate between layers, resident cells are displaced to the left and to the right, thus causing the deep cell layer to extend laterally (Fig. 3). Cells in the bottom deep cell layer are capable of depositing and assembling FN, and the incorporation of a rule to govern this behavior is discussed in more detail below.

Cells from the superficial cell layer do not intercalate into deep cell layers and cells in the deep cell layer do not intercalate into the superficial cell layer (Keller 1978, 1980; and unpublished experimental observations). Instead, the superficial cell layer conforms to the geometry of the deep layer cells by spreading laterally. As the deep layer cells intercalate between other deep

Table 1
Variables and rules for cell behavior obtained from published data and from experimental observations

	Parameter	Definition	Reference
Superficial cell layer	Cell size	25 × 25 μm	(Keller, 1980)
	Movement	The superficial cell layer provides a natural boundary by conforming to the geometry of deep layer cells. No cells from the superficial cell layer move into deep cell layers.	(Keller, 1978, 1980)
	Extension	The superficial cell layer extends laterally to cover the extending deep layers.	(Keller, 1978)
	Cell-to-cell contact	The cells in the superficial layer form a continuous epithelial sheet without intercellular spaces.	(Keller, 1978)
Inner deep cell layers	Cell size	25 × 25 μm	(Keller, 1980)
	Intercalation	Deep layer cells can intercalate into an upper or lower layer of deep cells; deep layer cells cannot intercalate into the superficial cell layer.	(Keller, 1978, 1980)
	Boundary capture	The bottom deep cell layer captures cells from inner deep cell layers that intercalate into the bottom deep cell layer.	(Marsden and DeSimone, 2001)
	Extension	Inner deep cell layers extend as cells intercalate.	(Keller, 1978, 1980)
	Cell-to-cell contact	Gaps in the inner deep cell layers are filled by inner deep cells above the gap or by the superficial cell layer, which conforms to the geometry of the deep cell layers.	(Keller, 1980)
Bottom deep cell layer	Cell size	25 × 25 μm	(Keller, 1980)
	Intercalation	Negligible; cells in the bottom deep cell layer cannot leave this cell layer.	(Marsden and DeSimone, 2001)
	Extension	The bottom deep cell layer extends as cells from the inner deep cell layers intercalate into the bottom layer.	(Keller, 1978, 1980)
	FN matrix deposition and assembly	Each cell in the bottom deep cell layer has a FN variable. The value of this variable is incremented at each time step if the cell has resided in the bottom layer for at least 30 min and the cell is in contact with cells that have also have a residency time of at least 30 min. If these criteria are not met, then the variable's value is reset to 0.	(Marsden and DeSimone, 2003; Winklbauer, 1998)
Timing	Clock variable	The clock is incremented by 1.87 min each time a deep layer cell intercalates into another layer. (This time increment is derived from the experimental observation that the bottom cell layer is "diluted" with intercalated cells by 20% after 1 h.)	Unpublished experimental observations
	Stage variable	Developmental stage is approximated by incrementing the stage variable by 1 every 60 min (stage = 8 when clock = 0 min).	(Keller, 1980; Nieuwkoop and Faber, 1994)

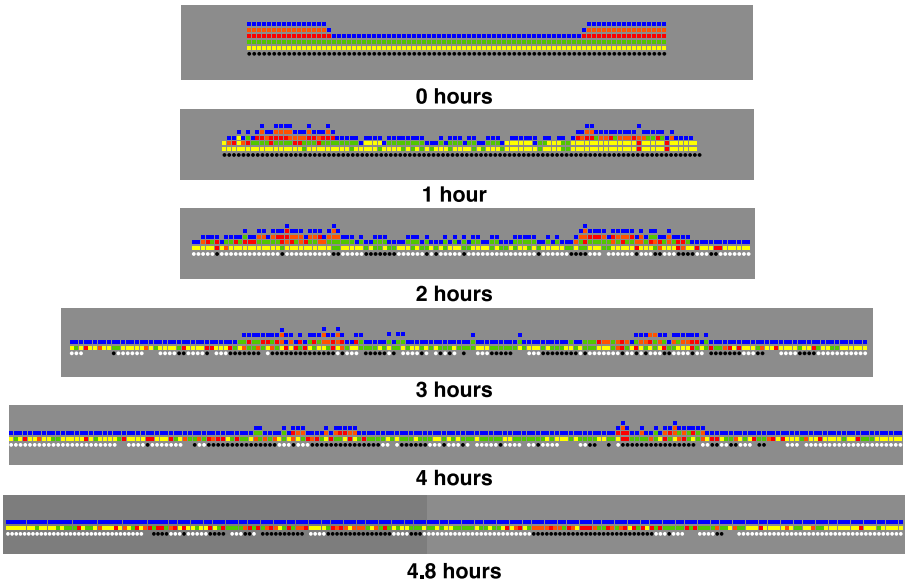

Fig. 3. Time sequence of the simulated process of BCR thinning in the *Xenopus laevis* embryo. The model begins with multiple cell layers and terminates when the inner deep cells (green, red, and orange blocks) have radially intercalated into the bottom layer of deep cells (yellow blocks). The radial intercalation of deep cell layers between one another leads to lateral extension, or elongation of the BCR. The superficial layer of cells (blue blocks) extends to cover the deep layer cells.

cell layers and the BCR lengthens, the superficial cell layer extends laterally to cover the extending deep cell layers.

A timing mechanism for cell intercalation rate was determined by measuring the dilution of the bottom cell layer in an embryo explant (see Materials and methods for more details). The experimental study produced data to suggest that the bottom cell layer is diluted with intercalating cells by approximately 20% after the first hour of thinning. A simulation clock was created by relating cell movement to the 20% dilution in the first hour. The amount of time elapsing between model clock increments, 1.87 min, was based on the calculated average time required for a single cell intercalation event. The model approximates the developmental stage by advancing the stage by one unit every 60 min. The simulation begins at developmental stage 8 and the clock is initialized to 0.

Emergent cellular rearrangement and tissue layer morphology replicated

The CA model successfully replicates the cell motions and final tissue morphology observed as the BCR thins in vivo. During the simulation, inner deep cells intercalate with one another and with the bottom deep cell layer to produce a BCR that is two cell layers thick (Fig. 3). The model begins (time = 0 h) with three to five cell layers (one layer of blue superficial cells and two to four cell layers of orange, red, green, and yellow deep cells). Over the next 4 h, the number of cell layers decreases as the deep cells intercalate radially and the BCR extends laterally. The simulation terminates (time = 4.8 h) when the BCR has thinned to a single layer of superficial cells completely covering a single layer of deep cells. This gradual reduction in the number of cell layers via radial intercalation has been described in vivo (Keller, 1980).

Total thinning time predicted

The CA model also recapitulates the timing of radial intercalation. The simulation predicts the total time necessary for morphogenetic thinning from the initial tissue geometry at stage 9 (0 h) to two cell layers (Fig. 3). The predicted thinning time of 4.79 ± 0.16 h is comparable to the experimentally observed BCR thinning time of approximately 4 h (Keller, 1980). Total thinning time was dependent on cell motions (Table 1) and independent experimental observations, discussed in more detail in Materials and methods. For example, inner deep layer cells are capable of intercalating into upper or lower cell layers. If the rules for the behavior of inner deep cells prevented cells from moving into upper cell layers and only allowed movement into lower cell layers, a different total thinning time would have been observed.

Lateral dispersion of implanted cells predicted

To further assess the predictive capabilities of the CA model, we incorporated microsurgical interventions and compared the predicted results of the simulation to an experimentally derived outcome based on actual in vivo manipulations. The intervention was generated in the simulation by implanting 10 cells under the superficial

layer (red cells in Fig. 4A). The 10 implanted cells responded to the same rules as those imposed on the rest of the inner deep layer cells by intercalating between other cells and other tissue layers, thus causing their dispersion in the radial and lateral directions throughout the thinning process. The metric used to assess the lateral dispersion of the implanted cells was the dispersion length ratio. This ratio was calculated by measuring the lateral dispersion, or the distance between the left-most and right-most implanted cells 1 h (denoted as *a*) and 5 h (denoted as *b*) after cell implantation (Figs. 4A and B, respectively). The average dispersion length ratio between these two time points was then calculated by dividing *b* by *a* for 25 simulation runs. For the 5-h/1-h time points, the CA simulation predicted an average dispersion length ratio of 1.9 ± 0.3.

Next, the independent experimental analog to this simulated microsurgical intervention was performed as diagrammed in Fig. 4C. Approximately 10 inner deep cells from a fluorescently labeled donor embryo were implanted just under the superficial layer at late stage 8–early stage 9 (Fig. 4C). As the BCR thinned in vivo, the implanted cells migrated with the host cells, intercalated between them, and became dispersed (or interspersed with host cells) along the lateral length of the thinned BCR. Initially in a round or oval shape (e.g., Fig. 4D), the aggregate of implanted cells expanded in all directions as the implanted cells intercalated between host cells (Fig. 4E). The lateral dispersion of implanted cells in the host BCR tissue was assessed in vivo 1 hour (Figs. 4F, *a* and G, *a*) and 5 h (at approximately stage 12; Figs. 4F, *b* and H, *b*) after implantation. Lateral dispersion lengths were defined as the distances along the long axis (shown) and short axis (not shown) of the oval implant between the left-most and right-most implanted cells 1 and 5 h after cell implantation. As in the simulation, the average dispersion length ratio was then calculated by dividing the dispersion length 5 h (*b*) after implantation by the dispersion length 1 h (*a*) after implantation (*b*/*a*; Fig. 4F). The 1-h post-implantation time point was chosen for

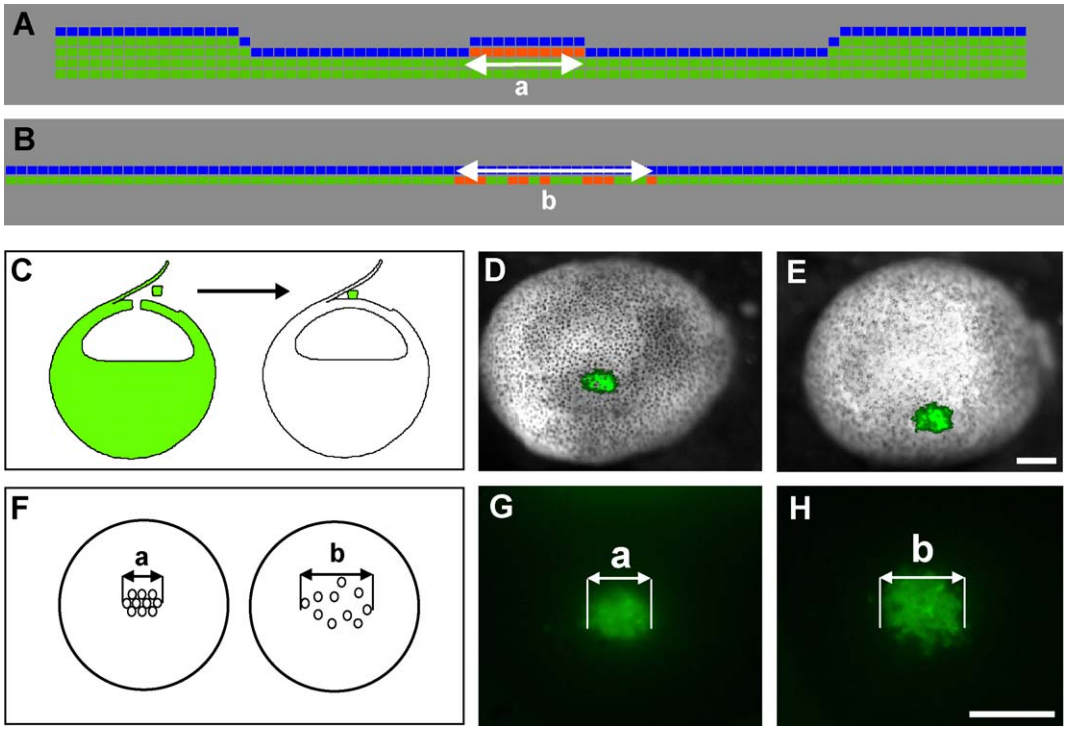

Fig. 4. The model predicts the lateral dispersion of implanted cells. To simulate the microsurgical implantation of a graft of labeled cells in the CA model, the initial morphology of the simulated BCR was modified by adding 10 extra deep cells (shown in red) (A). The length of the implanted patch, measured as the distance between the end cells, late in stage 8/early in stage 9 is represented by *a*. The simulation predicts the spatial fate of the implanted cells 5 h later (B). The maximum distance between cells at this time point is represented by *b*. The dispersion length ratio is calculated by dividing *b* by *a*. The simulation predicts a dispersion length ratio of 1.9 ± 0.3 (n = 25 simulation runs). The schematic of the analogous experimental manipulation shows how a homotypic, homochronic graft of deep cells from an alexa-488 dextran-labeled donor embryo was implanted into an unlabeled host embryo late in stage 8/early stage 9 (C). Fluorescence image overlaid onto a visible light image of cells grafted into a pigmented embryo late in stage 8–early in stage 9 (D), and 5 h later (E) (scale bar = 30 μm). The length of the implant (maximum distance between implanted cells) was measured along the long axis of the oval-shaped implant (F), late in stage 8–early in stage 9 (denoted as *a*) and 5 h later (denoted as *b*) and similarly along the short axis of the oval-shaped implant (perpendicular to *a* and to *b*). Fluorescence images of cells grafted into an albino embryo collected in the FITC channel immediately after implantation late in stage 8/early in stage 9 (G) and 5 h later (H) (scale bar = 30 μm). The ratio of *b* to *a* represents the dispersion length, and the average experimental dispersion length ratios measured along the long axis and short axis of the oval-shaped implants were 1.6 ± 0.5 and 1.7 ± 0.3, respectively (n = 6 embryos).

analysis to reduce possible effects of an initial wound healing response (Davidson et al., 2002). Six out of eight embryos experienced dispersion ratios greater than 1 (i.e., their dispersion length at the 5-h time point was greater than their dispersion length at the 1-h time point) and the data points from these six samples were incorporated into the average values of 1.6 ± 0.5 and 1.7 ± 0.3 for the long and short axes of the oval shaped implant, respectively. We suggest that the ratios for the long and short axes are relatively similar due to the isotropic natures of the intercalation and dispersion processes during BCR thinning. The observed similarity in the long and short axis dispersion ratio supports the validity of approximating three-dimensional tissue morphogenesis with a two-dimensional tissue structure in the simulation. The two embryos that did not have dispersion ratios greater than 1 were assumed to have experienced wound healing responses that caused abnormal cell clustering (Davidson et al., 2002).

Without altering the governing parameters and rules of the CA simulation, we simulated a microsurgical intervention and the CA model was capable of independently predicting the outcome. The simulation predicted an average dispersion length ratio of 1.9 ± 0.3, and this value was statistically similar to the average dispersion length ratios calculated for the experimentally manipulated embryos (1.6 ± 0.5 and 1.7 ± 0.3) ($P < 0.05$). This lends support for the predictive nature of the CA model of BCR thinning.

Robustness with respect to cell rearrangement and dispersion

To analyze the capacity of the CA model to remain stable when perturbations are introduced, we simulated microsurgical implantations of varying sizes, including 5, 10, 20, and 30 cells. The dispersion length ratio changed minimally as implant size varied. For example, when an implant of 5 cells was inserted beneath the superficial layer the ratio was 1.9 ± 0.3, compared to a 10-cell implant (1.9 ± 0.3), 20-cell implant (2.2 ± 0.3), and 30 cell-implant (2.2 ± 0.2). The fact that this ratio is statistically similar across varying implantation sizes illustrates the robustness of the model with respect to this outcome metric.

Fibronectin matrix assembly predicted

As the cells of the BCR intercalate during thinning, a matrix of FN is assembled at the interface of the inner layer of cells and the blastocoel (Lee et al., 1984; Winklbauer and Stoltz, 1995). The FN matrix is thought to play an instructive role in the BCR thinning process and is suggested to be required for normal tissue morphogenesis (Marsden and DeSimone, 2001). However, the mechanisms underlying matrix assembly and FN fibrillogenesis are not currently known. We hypothesize that FN matrix assembly and fibrillogenesis are direct results of cell–cell contact in the bottom deep cell layer, and require (1) a minimum bottom deep cell-to-bottom deep cell contact time of 30 min and (2) differential

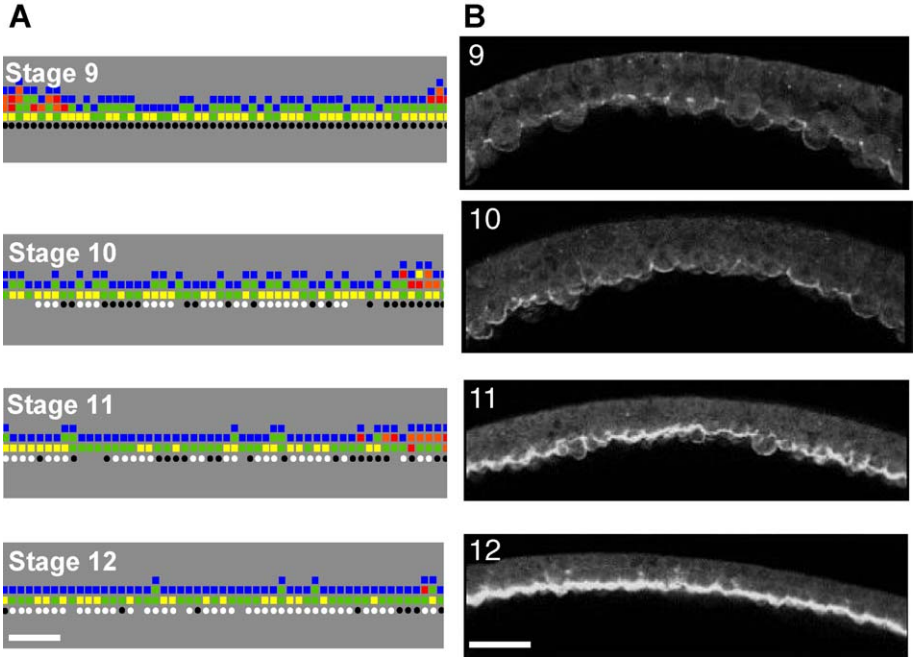

Fig. 5. The Model Predicts FN Matrix Assembly. (A) CA simulation prediction of FN intensity at stages 9, 10, 11, and 12 (scale bar = 100 μm). The bottom layer in the model is a grayscale representation of FN intensity. Black corresponds to negligible FN and white corresponds to the highest relative value of FN. (B) Photomicrographs of the BCR roof at stages 9, 10, 11, and 12 (scale bar = 100 μm). Bright white areas indicate high levels of FN. At each time point, the FN content is homogeneous and uniform across the entire area of the BCR; therefore, the sections in (B) are representative of the entire BCR area, in terms of FN content.

adhesion to the FN substrate, which causes cells to remain in the bottom deep cell layer after intercalating to this position. This hypothesis was based on experimental observations of embryo explants and the time required for FN matrix assembly in these explants (Marsden and DeSimone, 2003) and the observation that assembly requires cells to have lateral contact and a free surface (Winklbauer, 1998). We used the CA model of BCR thinning to test this hypothesis by incorporating the proposed rules into the CA model, running a series of simulations, analyzing predicted FN synthesis and assembly, and comparing that value to experimentally measured FN densities at different time points.

The CA model was adapted to include an algorithm for the deposition and assembly of FN fibrils based on our hypothesis. Specifically, each simulated cell in the bottom deep cell layer was given a FN variable. The value of this variable was incremented at each time step if the cell resided in the bottom layer for a minimum of 30 min and if the cell was in contact with neighboring cells that also had residency times of at least 30 min. Cells migrating or intercalating to the bottom deep cell layer remained there throughout the remainder of the simulation, captured by the developing FN substrate. The CA model recorded the level of the FN variable for each simulated cell throughout the duration of the simulation run, and the color of the FN layer was gray-scaled to reflect the level of this variable at every pixel spanning the underside of the bottom deep cell layer.

Using this algorithm, the CA model predicted the relative intensity of the FN matrix assembled on the underside of the BCR. The CA simulation showed an increase in FN content through stages 9, 10, 11, and 12 (Fig. 5A), which qualitatively resembled increased FN density in vivo throughout these stages (Fig. 5B). Using image analysis of confocal sections collected transverse to the BCR at each stage (see Materials and methods), we compared the predicted FN content to the experimentally observed FN content (Fig. 6A). To scale the predicted data to the experimentally measured data for the sake of comparing the two data sets, we normalized the simulation's level of FN at stage 11 to the experimental mean intensity level measured at this stage. Overall, there was a strong positive correlation (correlation coefficient = 0.9211) between the model's predicted FN values and the experimentally observed FN values (Fig. 6B). Thus, our simulation captures both the qualitative and quantitative features of FN fibril assembly in the BCR, and suggests that there is validity in our proposed hypothesis for FN synthesis and fibrillogenesis.

The largest difference between predicted and experimentally measured FN levels is seen at stage 10. At this stage, the predicted level is approximately 50% larger than the experimentally observed level. In the simulation, the predicted total FN levels are representative of fibrillar FN. At stage 11, FN assembly into fibrils is well underway in vivo, and therefore, we normalized the simulation's FN levels at this stage to the experimental FN intensity level at stage 11. However, between stages 8 and 10 in vivo, BCR cells have

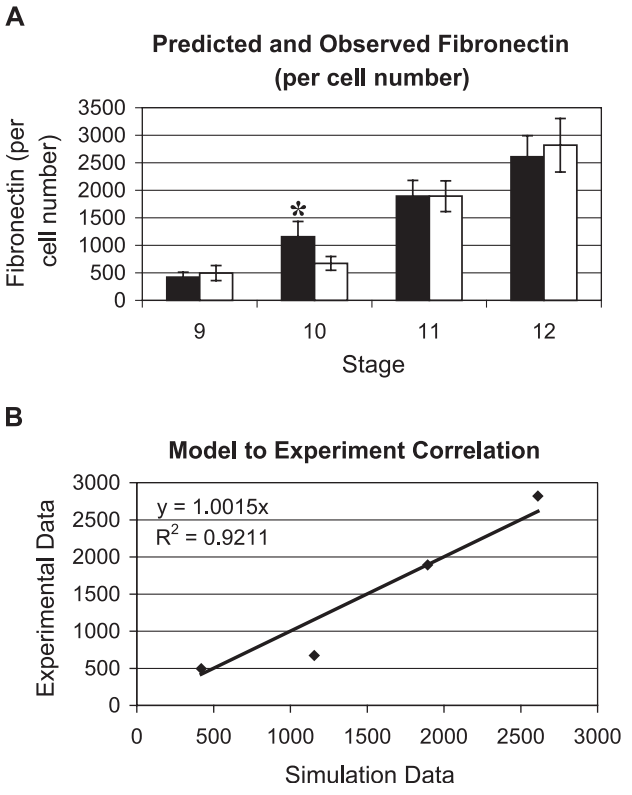

Fig. 6. Relationship between predicted FN content and experimentally observed FN content. (A) The predicted values of FN content were obtained from the output of the simulation (black bars). The observed values (white bars) were obtained by using Scion Image to analyze images of the BCR roof stained for FN. The FN values from the simulation were scaled so the mean predicted value would equal the mean observed value at stage 11 (* = statistically different from experimentally observed at that time point, $P < 0.05$). (B) There is a strong positive correlation between the model's predicted FN values and the experimentally observed FN values (correlation coefficient = 0.9211).

begun to deposit FN on their surfaces, but they have not yet initiated fibril polymerization and assembly. Thus, some of the in vivo FN during these stages is in a non-fibrillar (diffuse) configuration, which makes fluorescent intensity comparisons with relatively brighter late-stage FN fibrils difficult. The limited amount of FN assembly occurring at stage 10 (relative to stage 11) in vivo could produce an observed underestimate in this value at stage 10, and thus explain the large discrepancy between predicted and observed FN levels at stage 10. This difference between experimentally observed and simulation-predicted FN content at stage 10 could also result from the fact that FN is incorporated into the matrix at a faster rate once nascent fibrils are already present. Currently, the simulation does not include a positive feedback-signaling loop for this process.

Experimental test of cell residency time and matrix deposition

One way to test the hypothesis that cell residency time is critical to matrix accumulation in the BCR is to run the

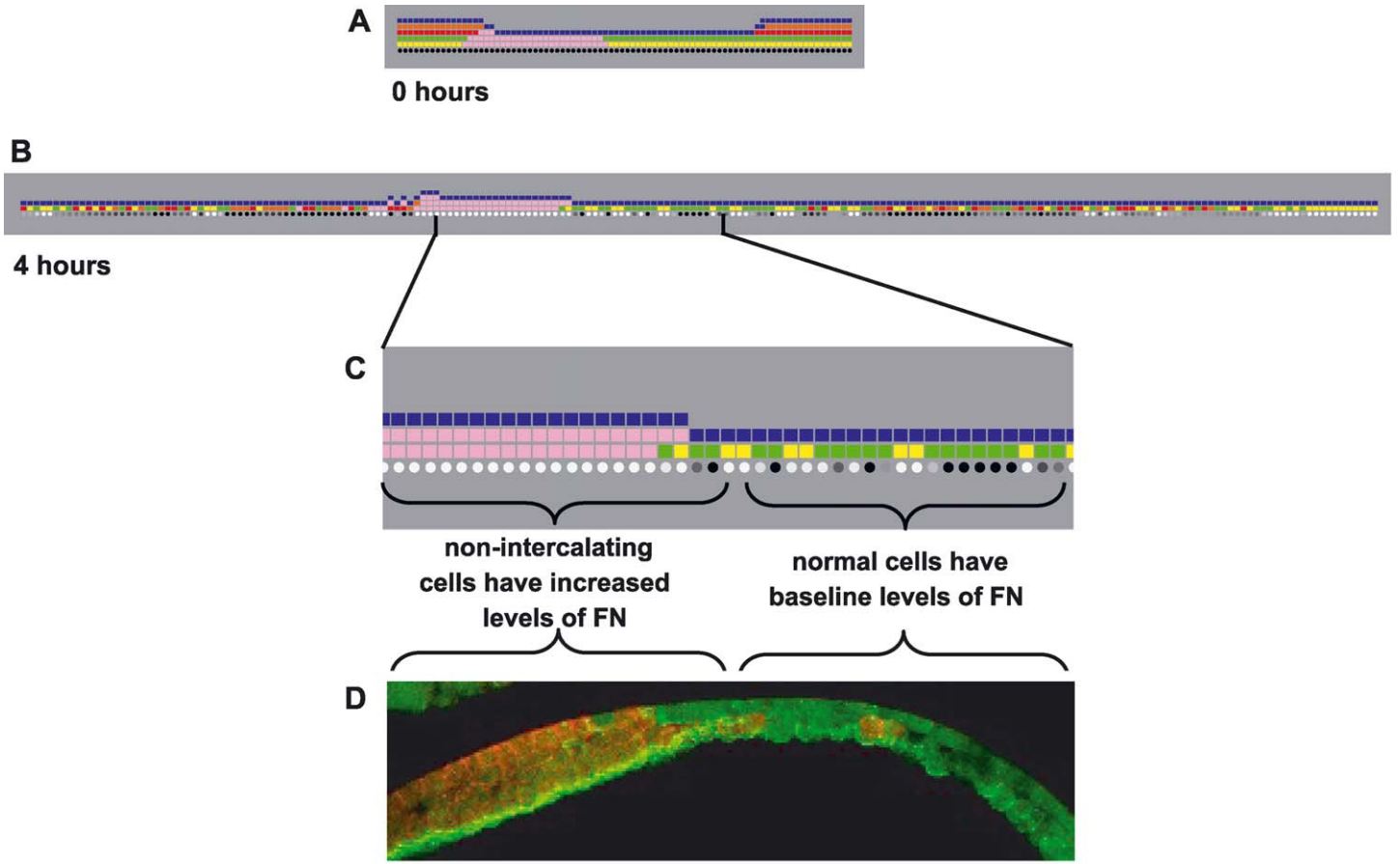

Fig. 7. Matrix accumulation increases with cell residency time. A patch of cells unable to undergo radial intercalation (non-intercalating cells, pink boxes) was simulated at $t = 0$ h (A) and $t = 4$ h (B). FN accumulation was simulated in both the patch and in neighboring cells that were free to undergo radial intercalation. Grayscale circles represent total FN accumulation at each time scale with white representing highest levels and black representing lowest levels (A–C). Enlargement in (C) corresponds to a portion of the simulation that is comparable in size to a region of the BCR in an intact embryo (D). Confocal section of BCR in (D) processed for immunolocalization of FN (green) and myc-tagged N-cadherin (red) in a patch of cells at stage 10+. FN accumulation is greatest under the N-cadherin expressing patch of cells, which also fail to rearrange and thin this region of the BCR. Neighboring cells in the BCR that lack N-cadherin thin normally and display significantly less FN at this stage.

CA model simulating a patch of cells that fails to undergo radial intercalation (Figs. 7A–C). Under these conditions, the model predicted that FN accumulation would increase significantly in the area of the patch but not in adjacent regions of the BCR (Fig. 7C). Our previous experimental studies demonstrated that monoclonal antibody inhibition of integrin binding to FN in BCR cells blocked radial intercalation (Marsden and DeSimone, 2001). However, these same reagents also block FN matrix assembly making them unsuitable to validate experimentally the relationship between increased residency time and FN accumulation revealed in the simulation (Figs. 7A–C). Another way to approach this problem, therefore, is to utilize a reagent predicted to block radial intercalation without directly interfering with the recognition of FN by integrin receptors on BCR cells. Cadherin adhesion has been proposed by us (Marsden and DeSimone, 2003) and others (Delarue et al., 1998; Keller et al., 2000) to play a central role in regulating cell intercalation behaviors. Indeed, experimental manipulations that either increase (Zhong et al., 1999) or decrease (Brieher and Gumbiner, 1994; Lee and Gumbiner, 1995) cell–cell adhesion mediated by cadherins have been shown to inhibit morphogenetic movements in *Xenopus*, presumably by preventing normal cell rearrangements.

As expected, patches of BCR cells over-expressing myc-tagged N-cadherin do not undergo radial intercalation. These thickened regions of the BCR reveal significant increases in FN matrix accumulation compared to adjacent regions of the BCR where N-cadherin is not expressed (Fig. 7D). Similar results were obtained following the over-expression of C- and E-cadherins (Dzamba and DeSimone, unpublished observations). Thus, a perturbation introduced into the CA simulation that increased cell residency time in the BCR by blocking radial intercalation predicted an increase in FN matrix accumulation that was subsequently verified by the results of a similar in vivo manipulation.

Discussion

The CA model presented here is capable of making important independent predictions about the *X. laevis* BCR thinning process, such as cellular rearrangement and tissue layer morphology, total time required for thinning, and lateral dispersion of implanted cells, all of which were verified by direct experimentation. We have also used the CA model to test and confirm a novel hypothesis relating differential cell adhesion and cell–cell contact status to FN deposition and fibrillogenesis at the cell surface. The multicellular approach offers a way to incorporate multiple signals, cell types, and cell–matrix interactions into complex morphogenetic processes.

Based on a set of rules obtained from the literature and from experimental observations, the CA model independently predicts emergent cellular rearrangements during BCR gastrulation that are consistent with those observed in vivo and in experimental embryo explants. Over a similar time course to that measured in vivo, cells in the simulation intercalate to produce a BCR that has thinned from 3 to 5 cell layers to two cell layers. In terms of cell layer morphology, the thinning of this simulated tissue mimics the thinning of the BCR in vivo.

The CA model was also successful in predicting the lateral dispersion of a patch of implanted cells. When cell patches of different sizes were implanted, they dispersed via cell intercalation through other cell layers, and their final locations in the simulated tissue were comparable to that observed in an analogous experimental manipulation. The average dispersions of cell implants of varying sizes were comparable to those measured in vivo, suggesting that the simulated cells exhibit realistic cell motions and that the CA model is robust with respect to such surgical manipulations.

Furthermore, the CA model was capable of incorporating a rule for FN matrix assembly that was formulated based on a hypothesized mechanism for this process in vivo. Based on published work, we hypothesized that the assembly of FN by the bottom cell layer of the BCR was dependent on a threshold cell residency time of 30 min (Marsden and DeSimone, 2003) that required cells to be in contact with the same cell neighbors for a minimum of 30 min before initiating FN matrix assembly. When this rule was incorporated into the CA simulation, a gradual increase in FN assembly was predicted that was comparable to that measured in vivo.

In an attempt to provide an experimental correlate to the cell residency requirement for matrix assembly, we utilized N-cadherin overexpression, which blocks BCR thinning but does not inhibit BCR cells from assembling FN. This was necessary because the other reagents we have used to block radial intercalation work by preventing the assembly of FN by the BCR (Marsden and DeSimone, 2001). The similarity between the simulated perturbation in radial intercalation and the experimentally derived data is dramatic (Fig. 7) and supports the CA model prediction nicely. These results reveal both the potential and current limitations of the CA model. While the N-cadherin experiment is consistent with the predicted outcome of the model by blocking radial intercalation, the precise molecular mechanism of action is unclear concerning matrix assembly. For example, cadherin over-expression may also affect cell signaling activities (e.g., changes in gene expression and/or cytoskeletal organization) that directly or indirectly influence integrin adhesion to FN. Further experimental studies will be needed to better understand the molecular mechanism of cadherin activity in this instance. On the other hand, the CA model offers considerable practical value by helping us to identify such issues, challenge emerging hypotheses and evaluate possible experimental strategies to distinguish among them.

In the context of blastocoel cell roof thinning, the prediction of the current CA model is important because it suggests that a minimal cell–cell contact time requirement and selective adhesion to a substrate are two cell behaviors that together are sufficient for generating FN assembly in the BCR. Furthermore, this prediction has important implications for developmental biology, in general, because it demonstrates how modeling can be used as a tool to link individual cell motions to tissue-level extracellular matrix assembly. Manipulating one or two aspects of behavior of individual cells within a whole tissue (i.e., controlling the amount of time required for a single cell in a specific location to initiate FN assembly) is feasible in such a computational model.

Several assumptions were made to simplify this initial CA model. For example, the model does not incorporate cell divisions and assumes that cell sizes and shapes remain constant throughout the BCR thinning process. Cells of the BCR in vivo undergo, at most, two cell divisions during the developmental stages modeled in this study (unpublished experimental observations) and thin and narrow along their radial axis as thinning progresses (Keller, 1980). However, our assumptions are likely valid because cell division in vivo (i.e., without growth) does not substantially alter total tissue area, length (i.e., in the two-dimensional CA model), or cell dispersion; any increases in frequency of cell division are compensated for by a concomitant reduction in cell size. The model also ignores changes in individual cell shapes, which may impact the overall areas and/or volumes occupied by the tissues of the BCR in vivo. Moreover, forces generated by additional morphogenetic processes in other regions of the embryo (e.g., convergence extension) may influence BCR thinning but there is currently no clear evidence that this is the case, at least in the region of the embryo that is modeled by the current simulation. Although some assumptions are necessary to simplify such a complex biological process, the accuracy of the model will improve as the number of assumptions incorporated in the model's design is decreased by newly acquired, experimentally derived metrics. Further modifications to the model may be necessary to realize fully the potential of the simulation method, but the computational nature of the CA model makes it highly accessible to modification, facilitates high throughput automated analysis, and rapidly generates useful data.

In conclusion, this study presents a CA model of one specific aspect of frog embryogenesis, BCR thinning during epiboly. The objective in developing this model was to analyze spatial and temporal patterns of BCR cell behaviors and FN matrix assembly during the morphogenetic thinning event. The results of this study suggest that a CA approach can be useful for investigating hypothesized underlying mechanisms responsible for epiboly and other cell rearrangements of gastrulation especially in instances where specific experimental strategies may not be immediately obvious. This particular cell-based computational model predicts important characteristics of epiboly including spatial and temporal aspects of emergent cell rearrangements, changes in tissue morphology, and extracellular matrix assembly.

Acknowledgments

Fund for excellence in science and technology (FEST) grant, Univ. of Virginia (to T.S. and D.W.D.); NIH HL-52309 and HL-65958 (to T.S.); NIH HD-26402 (to D.W.D.).

References

Brieher, W.M., Gumbiner, B.M., 1994. Regulation of C-cadherin function during activin induced morphogenesis of *Xenopus* animal caps. J. Cell Biol. 126, 519–527.

Brodland, G.W., Chen, H.H., 2000. The mechanics of heterotypic cell aggregates: insights from computer simulations. J. Biomech. Eng. 122, 402–407.

Brodland, G.W., Clausi, D.A., 1994. Embryonic tissue morphogenesis modeled by FEM. J. Biomech. Eng. 116, 146–155.

Chalmers, A.D., Strauss, B., Papalopulu, N., 2003. Oriented cell divisions asymmetrically segregate aPKC and generate cell fate diversity in the early *Xenopus* embryo. Development 130, 2657–2668.

Davidson, L.A., Ezin, A.M., Keller, R., 2002. Embryonic wound healing by apical contraction and ingression in *Xenopus laevis*. Cell Motil. Cytoskeleton 53, 163–176.

Delarue, M., Saez, F.J., Boucaut, J.C., Thiery, J.P., Broders, F., 1998. Medial cell mixing during axial morphogenesis of the amphibian embryo requires cadherin function. Dev. Dyn. 213, 248–260.

Evan, G.I., Lewis, G.K., Ramsay, G., Bishop, J.M., 1985. Isolation of monoclonal antibodies specific for human c-*myc* proto-oncogene product. Mol. Cell. Biol. 5, 3610–3616.

Honda, H., 1983. Geometrical models for cells in tissues. Int. Rev. Cytol. 81, 191–248.

Jacinto, A., Martinez-Arias, A., Martin, P., 2001. Mechanisms of epithelial fusion and repair. Nat. Cell Biol. 3, E117–E123.

Kay, B.K., Peng, H.B., 1991. *Xenopus laevis*: Practical Uses in Cell and Molecular Biology Academic Press, New York.

Keller, R.E., 1978. Time-lapse cinemicrographic analysis of superficial cell behavior during and prior to gastrulation in *Xenopus laevis*. J. Embryol. Exp. Morphol. 157, 223–248.

Keller, R.E., 1980. The cellular basis of epiboly: an SEM study of deep-cell rearrangement during gastrulation of *Xenopus laevis*. J. Embryol. Exp. Morphol. 60, 201–234.

Keller, R., Davidson, L., Edlund, A., Elul, T., Ezin, M., Shook, D., Skoglund, P., 2000. Mechanisms of convergence and extension by cell intercalation. Philos. Trans. R. Soc. London, B Biol. Sci. 355, 897–922.

Lee, C.H., Gumbiner, B.M., 1995. Disruption of gastrulation movements in *Xenopus* by a dominant-negative mutant for C-cadherin. Dev. Biol. 171, 363–373.

Lee, G., Nynes, R., Kirschner, M., 1984. Temporal and spatial regulation of fibronectin in early *Xenopus* development. Cell 36, 729–740.

Marsden, M., DeSimone, D.W., 2001. Regulation of cell polarity, radial intercalation and epiboly in *Xenopus*: novel roles for integrin and fibronectin. Development 128, 3635–3647.

Marsden, M., DeSimone, D.W., 2003. Integrin-ECM interactions regulate cadherin-dependent cell adhesion and are required for convergent extension in *Xenopus*. Curr. Biol. 13, 1182–1191.

Martin, P., Wood, W., 2002. Epithelial fusions in the embryo. Curr. Opin. Cell Biol. 14, 569–574.

Meinhardt, H., Gierer, A., 1980. Generation and regeneration of sequence of structures during morphogenesis. J. Theor. Biol. 85, 429–450.

Metzger, R.J., Krasnow, M.A., 1999. Genetic control of branching morphogenesis. Science 284, 1635–1639.

Murray, J.D., Oster, G.F., 1984. Cell traction models for generating pattern and form in morphogenesis. J. Math. Biol. 19, 265–279.

Ngwa, G.A., Maini, P.K., 1995. Spatio-temporal patterns in a mechanical model for mesenchymal morphogenesis. J. Math. Biol. 33, 489–520.

Nieuwkoop, P.D., Faber, J., 1967. Normal Tables of *Xenopus laevis*. Elsevier/North-Holland Biomedical Press, Amsterdam.

Nieuwkoop, P.D., Faber, J., 1994. Normal Table of *Xenopus laevis.* Garland Publishing, Inc., London.

Peirce, S.M., Van Gieson, E.J., Skalak, T.C., 2004. Multicellular simulation predicts microvascular patterning and in silico tissue assembly. FASEB J. 18, 731–733.

Sater, A.K., Steinhardt, R.A., Keller, R., 1993. Induction of neuronal differentiation by planar signals in *Xenopus* embryos. Dev. Dyn. 197, 268–280.

Simske, J.S., Hardin, J., 2001. Getting into shape: epidermal morphogenesis in *Caenorhabditis elegans* embryos. BioEssays 23, 12–23.

Sive, H.L., Grainger, R.M., Harland, R.M. (Eds.), 2000. Early development of *Xenopus laevis*: a laboratory manual. Cold Spring Harbor Laboratory Press, New York.

von Dassow, G., Meir, E., Munro, E.M., Odell, G.M., 2000. The segment polarity network is a robust developmental module. Nature 406, 188–192.

Weliky, M., Oster, G., 1990. The mechanical basis of cell rearrangement. I. Epithelial morphogenesis during Fundulus epiboly. Development 109, 373–386.

Weliky, M., Minsuk, S., Keller, R., Oster, G., 1991. Notochord morphogenesis in *Xenopus laevis*: simulation of cell behavior underlying tissue convergence and extension. Development 113, 1231–1244.

Winklbauer, R., 1998. Conditions for fibronectin fibril formation in the early *Xenopus* embryo. Dev. Dyn. 212, 335–345.

Winklbauer, R., Stoltz, C., 1995. Fibronectin fibril growth in the extracellular matrix of the *Xenopus* embryo. J. Cell Sci. 108, 1575–1586.

Zajac, M., Jones, G.L., Glazier, J.A., 2003. Simulating convergent extension by way of anisotropic differential adhesion. J. Theor. Biol. 222, 247–259.

Zhong, Y., Brieher, W.M., Gumbiner, B.M., 1999. Analysis of C-cadherin regulation during tissue morphogenesis with an activating antibody. J. Cell Biol. 144, 351–359.